

# The Amount of Recycled Crust in Sources of Mantle-Derived Melts

Alexander V. Sobolev,<sup>1,2\*</sup> Albrecht W. Hofmann,<sup>1</sup> Dmitry V. Kuzmin,<sup>1,3</sup> Gregory M. Yaxley,<sup>4</sup> Nicholas T. Arndt,<sup>5</sup> Sun-Lin Chung,<sup>6</sup> Leonid V. Danyushevsky,<sup>7</sup> Tim Elliott,<sup>8</sup> Frederick A. Frey,<sup>9</sup> Michael O. Garcia,<sup>10</sup> Andrey A. Gurenko,<sup>1</sup> Vadim S. Kamenetsky,<sup>7</sup> Andrew C. Kerr,<sup>11</sup> Nadezhda A. Krivolutsкая,<sup>2</sup> Vladimir V. Matvienkov,<sup>12</sup> Igor K. Nikogosian,<sup>13,14</sup> Alexander Rocholl,<sup>15</sup> Ingvar A. Sigurdsson,<sup>16</sup> Nadezhda M. Sushchevskaya,<sup>2</sup> Mengist Teklay<sup>17</sup>

Plate tectonic processes introduce basaltic crust (as eclogite) into the peridotitic mantle. The proportions of these two sources in mantle melts are poorly understood. Silica-rich melts formed from eclogite react with peridotite, converting it to olivine-free pyroxenite. Partial melts of this hybrid pyroxenite are higher in nickel and silicon but poorer in manganese, calcium, and magnesium than melts of peridotite. Olivine phenocrysts' compositions record these differences and were used to quantify the contributions of pyroxenite-derived melts in mid-ocean ridge basalts (10 to 30%), ocean island and continental basalts (many >60%), and komatiites (20 to 30%). These results imply involvement of 2 to 20% (up to 28%) of recycled crust in mantle melting.

It is widely accepted that the heterogeneity of the convecting mantle observed in the composition of mantle-derived magmas is largely due to subduction and recycling of oceanic crust into the deep mantle (1, 2). To understand the role of crustal material in creating compositional heterogeneities in the mantle and to evaluate the geodynamical consequences of this contribution, one must quantify the crustal

input to the mantle sources of common, mantle-derived magmas in mid-oceanic ridges basalts (MORBs), ocean islands (OIBs), and large igneous provinces (LIPs). It is not possible to use incompatible element abundances in basalts to constrain the proportion of recycled component in the magma source because concentrations of these elements are also sensitive to the extent of melting. Similarly, the use of isotope ratios for making such quantitative estimates is compromised by the isotopic variability of subducted materials involved in the recycling process (2). We used an alternative approach based on a combination of major elements and compatible trace elements in parental melts, because these are more uniform in the mantle and are strongly controlled by the residual phases in equilibrium with partial melts (3–5).

Our method has its basis in the experimental and theoretical prediction that high-pressure ( $P > 3.0$  GPa) melting of typical recycled oceanic crust (in the form of eclogite with a separate  $\text{SiO}_2$  phase) and reaction of this melt with peridotite produces olivine-free pyroxenite (5). We show that further melting of this hybrid lithology in the absence of residual olivine is more voluminous than the melting of peridotite (at a given pressure and temperature) and that pyroxenite-derived melts are characteristically enriched in Si and Ni but depleted in Mg, Ca, and Mn compared with their peridotite-derived counterparts. This difference arises because olivine principally controls the composition of melt produced in peridotite, whereas pyroxene mainly controls the composition of melt from olivine-free hybrid pyroxenite (5–8). Experimental data predict (9) that, as such pyroxenite-derived melts rise toward the surface, the decrease in pressure causes their saturation in olivine. This olivine is unusually Ni rich and Mn and Ca poor. With use of a new, large data set of high-precision analyses of

olivine phenocrysts from OIBs, LIPs, MORBs, and komatiites, we show that hybrid pyroxenite is a common lithology in upwelling mantle and a major contributor to tholeiitic (silica-saturated) and transitional (moderately silica-undersaturated) magmas of OIBs and LIPs emplaced on thick oceanic or continental lithosphere.

**Olivine data set.** We use olivine phenocrysts as probes of parental melt composition, because olivine is the first phase to precipitate at low pressures in almost all mantle-derived magmas and because its forsterite content is an excellent measure of the degree of fractional crystallization allowing reconstruction of the parental melt composition.

Olivine phenocrysts were analyzed by electron microprobe using high probe currents and long counting times (10). This procedure routinely yields detection limits of around 6 to 15 parts per million (ppm) and errors (2 standard errors) of 15 to 30 ppm for trace elements (Ni, Ca, Mn, Cr, Co, and Al) and 0.01 mole percent (mol %) for forsterite content [defined as  $\text{Fo} = \text{Mg}/(\text{Mg} + \text{Fe})$ ], checked by repeated analysis of San Carlos olivine standard (11). In the following diagrams we use only high-precision data.

We have analyzed nearly 17,000 grains of olivine phenocrysts from 229 samples of tholeiitic to transitional compositions covering MORBs (40 samples) from Mid-Atlantic Ridge, East Pacific Rise, South-East Indian Ridge, and Knipovich Ridge; OIBs (138 samples) from Hawaiian Islands and Emperor Seamounts, Canary Islands, Reunion, Azores, and Iceland; LIPs (36 samples) from Ontong Java Plateau, Siberia, Emeishan, Karoo, Afar, and North Atlantic Province; komatiites and associated picrites (15 samples) from the Archean Abitibi greenstone belt in Canada and the Belingwe belt in Zimbabwe and South Africa; Proterozoic komatiitic basalts from Gilmour Island, Canada; and komatiites and picrites from Gorgona Island, Colombia. Most samples are picrites or olivine basalts containing large amounts of fresh, high-magnesium olivine phenocrysts. The samples are subdivided into four groups: (i) MORB; (ii) within plate magmas (WPM, magmas erupted far from plate boundaries) forming OIB emplaced over thin lithosphere (<70 km thick), WPM-THIN; (iii) WPM (OIB and LIP) emplaced over thick lithosphere (>70 km thick), WPM-THICK; and (iv) komatiites and associated magmas, KOMATIITES. Details of sample locations, references for sample descriptions, and their group correspondence are presented in table S2a.

The most-magnesian olivine compositions (defined by olivines phenocrysts with Fo within 1 mol % from a maximum Fo) for each specimen were averaged (table S2a) for the plots shown in Fig. 1. Individual olivine analyses are presented on fig. S4 and tables S2, c to f.

In addition to Mn and Ni concentrations, which strongly correlate with Fo (Fig. 1, A and

<sup>1</sup>Max Planck Institute (MPI) for Chemistry, Post Office Box 3060, 55020 Mainz, Germany. <sup>2</sup>Vernadsky Institute of Geochemistry and Analytical Chemistry, Russian Academy of Sciences, Kosygin Street 19, 119991 Moscow, Russia. <sup>3</sup>Institute of Geology and Mineralogy, Siberian Branch of Russian Academy of Sciences, Koptuyga prospekt 3, 630090 Novosibirsk, Russia. <sup>4</sup>Research School of Earth Sciences, Australian National University, Canberra, ACT 0200 Australia. <sup>5</sup>Laboratoire de Géodynamique des Chaînes Alpines, Université de Grenoble, 38401 Grenoble cedex, France. <sup>6</sup>Department of Geosciences, National Taiwan University, Post Office Box 13-318, Taipei 106, Taiwan. <sup>7</sup>Australian Research Council, Centre of Excellence in Ore Deposits and School of Earth Sciences, University of Tasmania, Private Bag 79, Hobart, Tasmania, 7001, Australia. <sup>8</sup>Department of Earth Sciences, Queen's Road, Wills Memorial Building, University of Bristol, Bristol BS8 1RJ, UK. <sup>9</sup>Department of Earth, Atmospheric, and Planetary Science, Massachusetts Institute of Technology (MIT), 77 Massachusetts Avenue, Cambridge, MA 02139, USA. <sup>10</sup>Department of Geology and Geophysics, University of Hawaii, 1680 East-West Road, Honolulu, HI 96822, USA. <sup>11</sup>School of Earth, Ocean and Planetary Sciences, Cardiff University, Main Building, Park Place, Cardiff CF10 3YE, UK. <sup>12</sup>P. P. Shirshov Institute of Oceanology of Russian Academy of Sciences, Nakhimovsky prospekt 36, 117997 Moscow, Russia. <sup>13</sup>Department of Petrology, Faculty of Geosciences Utrecht University, Budapestlaan 4, Utrecht, Netherlands. <sup>14</sup>Department of Petrology, Faculty of Earth and Life Sciences, Vrije Universiteit, De Boelelaan 1085, 1081 HV Amsterdam, Netherlands. <sup>15</sup>Department of Earth and Environmental Sciences, University Munich, 80333 Munich, Germany. <sup>16</sup>South Iceland Nature Centre, Strandvegur 50, Vestmannaeyjar, IS 900, Iceland. <sup>17</sup>Department of Earth Science, University of Asmara, Asmara, Eritrea.

\*To whom correspondence should be addressed. E-mail: sobolev@geokhi.ru

C), we also plot Mn/Fe and Ni versus Mg/Fe ratios (Fig. 1, B and D). These ratios do not vary significantly with olivine fractionation (see model curves Frac 1 and Frac 2) but nevertheless range considerably (Fig. 1, B and D). Most olivine phenocrysts from MORBs and many from komatiites have Mn and Ni contents similar to those of peridotite-derived melts. In contrast, most olivines from the WPM-THICK group are significantly depleted in Mn and enriched in Ni. Their concentrations are not compatible with the melting products of common peridotites. The olivines from the WPM-THIN group have intermediate Mn and Ni contents.

Concentrations of Ca also provide some discrimination in spite of the greater overlap. Most olivines from the WPM-THICK group are too low in Ca to have precipitated from peridotite-derived melts (shown as experimental-based model compositions and fractionation trajectories, Fig. 1E).

Chromium is strongly controlled by garnet and spinel in peridotites and thus might be useful to decipher products of high-degree melting of

peridotite, which leave residuals (restites) free of Cr-rich phases (12). Olivines from Archean komatiites have the highest Cr values and match compositions of olivines from a spinel- and garnet-free refractory restite (Fig. 1F). They could, therefore, be derived directly from high-degree melting of peridotite. In the other groups of olivines, Cr is markedly lower than expected in equilibrium with peridotite at high pressures (see experimental data on lherzolite melting, Fig. 1F). The lowest Cr contents are found in MORB olivines, indicative of residual Cr spinel.

Cobalt (Fig. 2A) shows nearly uniform correlation with Fo for all rock groups, with possibly only minor (around 5%) relative enrichment in WPM-THICK and WPM-THIN over MORB (estimated from group average Co/Fe of table S2a). Decoupling of Co and Ni yields Ni/Co ratios of many WPM-THICK olivines that are unusually high for the Earth mantle (Fig. 2B).

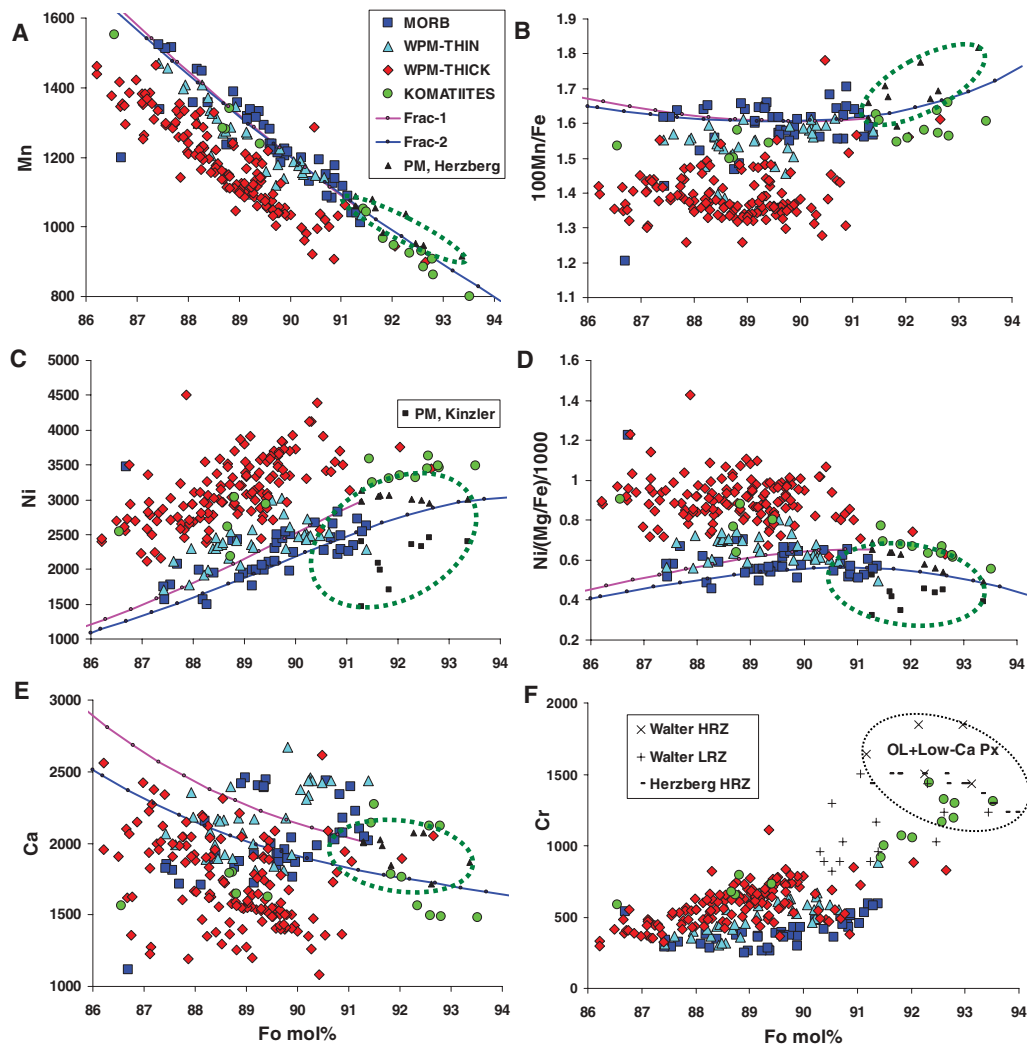
Mn/Fe is the parameter least dependent on olivine fractionation (as shown by the model fractionation curves in Fig. 3). Thus, it is diagnostic of parental magma compositional differ-

ences. There is a significant negative correlation of Ni/Mg versus Mn/Fe (linear correlation coefficient  $r$  is 0.66 for 238 samples) in spite of strong dependence of Ni/Mg on the degree of olivine fractionation (see fractionation trajectories in Fig. 3A). This correlation improves ( $r = 0.88$  for 103 samples) for the subset of olivines with a narrower range of Fo contents (Fo89 to Fo91). MORB olivines are the lowest in Ni and highest in Mn, whereas olivines from the WPM-THICK group are the highest in Ni and lowest in Mn, with olivines from the WPM-THIN group being intermediate.

To minimize the effects of olivine fractionation, we show parameters Ni/(Fe/Mg) and Ca/Fe in Fig. 3, B and C. This procedure also reduces the scatter in the ordinate significantly, thus highlighting the differences between geodynamic settings.

**Fate of recycled oceanic crust.** In subduction at  $P > 2.5$  GPa, the basaltic and gabbroic portions of the oceanic crust are transformed completely to eclogite (clinopyroxene and garnet) with a free SiO<sub>2</sub> phase (13–15). Unless silica has been

**Fig. 1.** (A to F) Average compositions of the most highly magnesian olivine phenocrysts in each sample. Concentrations and their ratios are given in ppm versus forsterite content of olivine in mol %. Olivine group names are as defined in text. PM, Herzberg indicates compositions of olivine in equilibrium at 0.1 MPa with melt originally generated at 3.0 to 5.0 GPa from fertile peridotite (12), calculated by Petrolog software (41) for oxygen fugacity corresponding to quartz-fayalite-magnetite (QFM) buffer using the Herzberg model (4), PM, Kinzler, olivine compositions similar to PM, Herzberg but with Ni calculated by using Ni partitioning between olivine and melt from Kinzler *et al.* (28). Frac 1 is the trend of olivine composition during fractional crystallization from a melt derived from fertile peridotite at 3 GPa and 1515°C (12). Fractionation of olivine modeled up to 20% for oxygen fugacity corresponding to QFM buffer using the Herzberg model (4). Frac 2 is similar to Frac 1 but calculated for 35% crystallization of melt derived at 4.0 GPa and 1630°C (12). Green ellipse indicates field of olivine compositions compatible with peridotitic source. In (F), HRZ, Herzberg stands for calculated compositions of olivine from spinel- and garnet-free harzburgite restite using (4); LHRZ, Walter and HRZ, Walter indicate experimental olivines from lherzolite- and garnet-free harzburgite residual assemblages, respectively, produced by high-pressure melting of fertile peridotite (12). Black ellipse marked "ol + low Ca-Px" indicates field of olivine compositions from refractory garnet- and spinel-free assemblage of olivine and low-Ca pyroxene.



removed during subduction (16), this combination will also be the relevant assemblage during recycling to the upper mantle (17).

In the ascending mantle (e.g., a mantle plume or upstream flow of convecting mantle), the silica-oversaturated eclogite starts melting at higher pressures than the peridotite and produces high silica melt (18, 19). This melt reacts with olivine from peridotite, producing pyroxenes and garnet (5, 8, 19). Previous studies have envisioned that this reaction creates a refertilized peridotite enriched in pyroxene (19, 20). This conclusion would predict variable mixing proportions of individual ingredients (eclogite-derived high-Si melt and peridotite) that are

drastically different in composition. Melting such variable source compositions would create highly nonlinear correlations of  $^{187}\text{Os}/^{188}\text{Os}$  and  $^{87}\text{Sr}/^{86}\text{Sr}$  isotope ratios in the melts, and this is contradicted by the strongly linear correlations observed in Hawaiian basalts (21, 22), which are thought to have a significant eclogite component (3, 5).

However, it has been shown experimentally (23) and proposed on the basis of Korzinskii's theory (24) that, under conditions of local equilibrium, the reaction between high-Si eclogite-derived melt and peridotite produces an olivine-free lithology enriched in pyroxene (5). This fundamentally differs from a partial reaction (19, 20) because it leads to a stable pyroxenite lithology (hybrid py-

roxenite) generated by roughly fixed proportions of high-Si melt and peridotite [constrained by reaction stoichiometry between 40 and 60 weight % (wt %) of melt (5)] irrespective of the initial proportions of the reaction ingredients. Consequently, the hybrid pyroxenite has nearly uniform chemical and isotopic composition, thus constituting a single mixing endmember. Binary mixing of melts derived from peridotite and this pyroxenite leads to near-linear  $^{87}\text{Sr}/^{86}\text{Sr}$  versus  $^{87}\text{Os}/^{188}\text{Os}$  trends (5).

Other predicted geochemical consequences of replacement of olivine by pyroxene are a significant decrease of the bulk distribution coefficient between crystals and melt ( $K_d$ ) for Ni

**Fig. 2. (A and B)** Cobalt and nickel to cobalt ratio versus Fo of average Mg-rich olivine phenocrysts. Pink band at Ni/Co  $20 \pm 1$  represents estimated values for bulk silicate Earth (BSE), core, and chondrites (39). Arrows indicate trend of olivine compositions due to the mantle melting (melting) and magma crystallization (cryst). All other symbols are as on Fig. 1.

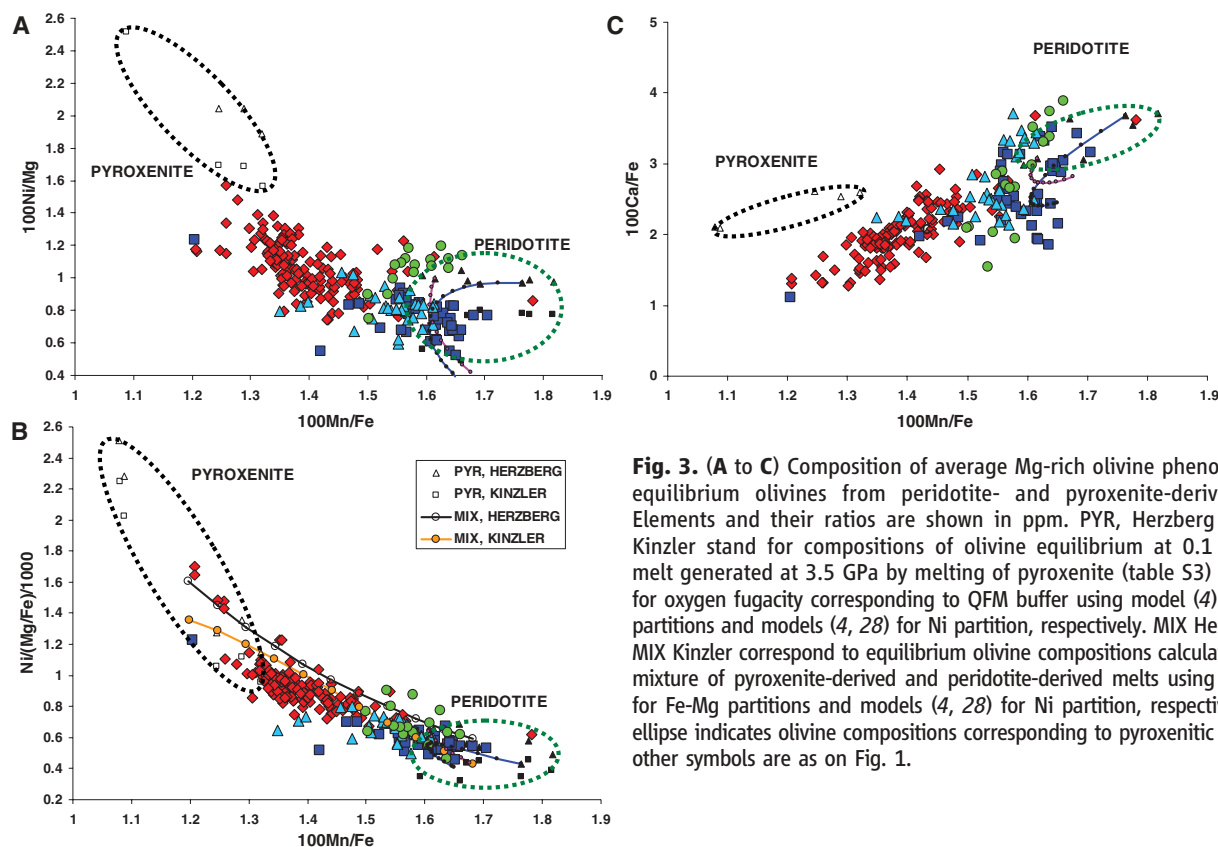
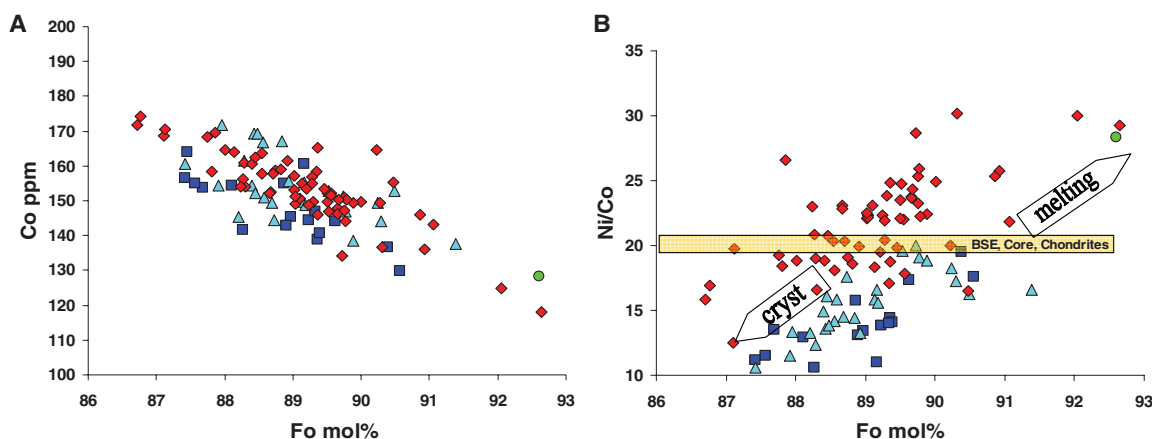


**Fig. 3. (A to C)** Composition of average Mg-rich olivine phenocrysts and equilibrium olivines from peridotite- and pyroxenite-derived melts. Elements and their ratios are shown in ppm. PYR, Herzberg and PYR, Kinzler stand for compositions of olivine equilibrium at 0.1 MPa with melt generated at 3.5 GPa by melting of pyroxenite (table S3) calculated for oxygen fugacity corresponding to QFM buffer using model (4) for Fe-Mg partitions and models (4, 28) for Ni partition, respectively. MIX Herzberg and MIX Kinzler correspond to equilibrium olivine compositions calculated for the mixture of pyroxenite-derived and peridotite-derived melts using model (4) for Fe-Mg partitions and models (4, 28) for Ni partition, respectively. Black ellipse indicates olivine compositions corresponding to pyroxenitic source. All other symbols are as on Fig. 1.

(5, 6) and a decrease in the ratio of the bulk coefficients of Mn and Fe (7). These features occur because olivine is the major silicate phase in peridotite concentrating Ni and the only silicate phase in peridotite having  $K_d$  for Fe greater than  $K_d$  for Mn (7). The bulk  $K_d$  changes will increase Ni and lower the Mn/Fe ratio of pyroxenite-derived melt compared with peridotite-derived melts. In addition, melting of pyroxenite yields lower Ca compared with peridotite (8). Additional predicted differences are higher melt fractions for hybrid pyroxenite than peridotite and higher Si and lower Mg in pyroxenite-derived melt (5, 25, 26).

These predictions were tested by experimental melting of a model hybrid pyroxenite (5). Experiments were run at  $P = 3.5$  GPa and temperatures between 1400° and 1570°C in a conventional 1.27-cm piston-cylinder apparatus at the Australian National University (10, 19). These results, together with published experimental data for melting of peridotite (12), confirm the Ni and Mn relationships as well as melting rates predicted above (table S3 and fig. S5). From these data, we calculate equilibrium olivine compositions at low pressure (4, 27, 28) in order to compare them with the natural phenocryst data (Fig. 3). We used these results to estimate mixing proportions of melts derived from the two end-member sources for the olivine data sets representing different geodynamic settings. The end-member melt compositions were calculated from averaging experimental data on melting of pyroxenite and peridotite (10).

**Quantitative estimates.** We assumed mixtures (in 10% intervals) of the end-member melts (10) and calculated the composition of equilibrium olivines. The calculated mixing trajectories for the two different models for Ni partitioning

are consistent with natural olivine data (Fig. 3B). The relation between Mn/Fe of modeled olivines and mixing proportions (10) was used to compute the amount of pyroxenite-derived component for individual samples (Fig. 4). Olivines from the WPM-THICK group of basalts yield an average of  $61 \pm 16\%$  (standard deviation) pyroxenite-derived component, similar to results derived from Ni contents in Hawaiian melt inclusions and olivines only (5). The olivines from some continental LIPs (specific suits from Siberia and Karoo) indicate almost pure pyroxenitic sources. Corresponding results for the other groups are for WPM-THIN,  $30 \pm 13\%$ ; for Archean komatiites,  $21 \pm 10\%$ ; and for MORB, excluding one unusual sample from the Southern Atlantic (see below),  $17 \pm 12\%$  [similar to predictions of (25)]. Because of the uncertainties involved in estimating the end-member compositions, the differences between groups are better constrained than the absolute numbers. Although MORBs contain the lowest proportion of pyroxenite-derived melt, the spread of MORB data is significant, and many samples do contain substantial amounts of pyroxenite-derived component [the extreme is the enriched in silica MORB sample from the Southern Atlantic (29) with 100% pyroxenite-derived component]. The calculations show that the Archean komatiites contain a significant amount of pyroxenitic component (maximum of 30% for samples from Canada and Belingwe), although the largest amount is in Proterozoic komatiitic basalts from Gilmour Island, Canada (up to almost 40%). From these calculations, an estimate of the amount of recycled oceanic crust (10) yields 4% for MORB, 11% for WPM-THIN group, 16% for WPM-THICK group, and around 13% for Archean komatiites. The highest estimate of

the amount of recycled oceanic crust (10) yield Ontong Java high-Mg lavas: 13% to 28%.

**Silica-undersaturated basalts.** Most of the magmas analyzed in this study are silica saturated (tholeiites or transitional). Only a few samples are moderately silica-undersaturated alkali magmas (e.g., Azores and Afar). Our database is representative of the normal oceanic crust, several of the world's major suites of flood basalts (LIPs), several of the major modern mantle plumes (30), and some komatiites. The strongly silica-undersaturated associations not covered here include continental rift basalts, many smaller ocean islands consisting mostly of alkali lavas, and also some larger-flux plumes (30) such as Pitcairn, Tahiti, and Cape Verde islands. Why are such basalts that are highly enriched in incompatible elements, and therefore presumably generated by very low degrees of melting, nearly always undersaturated in silica? This observation appears to contradict our model; one would expect that silica-saturated melts generated from hybrid pyroxenites should be prevalent, especially at very low melt fractions. There are several possible explanations. (i) A volatile (mostly  $\text{CO}_2$ -) triggered melting of peridotite may be the dominant mechanism forming strongly silica-undersaturated alkaline magmas at temperatures lower than hybrid pyroxenite melts (31). (ii) Low-degree melts of silica-saturated eclogite may be retained in the source because of their high viscosity, thus preventing production of the hybrid pyroxenite (5). (iii) Melting of hybrid pyroxenite at the contact with peridotite may produce low-degree, silica-undersaturated melts at lower temperatures than melting of hybrid pyroxenite itself (8). (iv) Melting of biminerally eclogites (no free silica phase) formed from silica-undersaturated recycled crust produces undersaturated alkaline magmas (16).

**What controls the amount of pyroxenite-derived melt?** By following the method outlined above, we estimated the proportions of melt derived from pyroxenite and peridotite for each parental magma. These proportions depend on several interrelated parameters, namely the thickness of lithosphere, the potential mantle temperature ( $T_p$ ) (32), and the amount of recycled crust in the upwelling mantle (Fig. 5). Because at the same  $T_p$  pyroxenite melts at higher pressure than peridotite (26), a thick lithosphere (which imposes a high lower limit on the depth of melting) will suppress low-depth peridotite melting and therefore favor a high proportion of pyroxenite-derived melts (33, 34). The extreme case is found in some continental flood basalts (specific suites of Siberia and Karoo at table S2a) where the amount of pyroxenite-derived melt is nearly 100%. In such a case, the amount of recycled material cannot be estimated because the peridotitic component contributes no melt. In contrast, a thin lithosphere (MORB, Iceland, Azores, and Detroit seamount) favors a higher proportion of peridotite-derived melt because of the increasing degree of melting of peridotite at shallower depths.

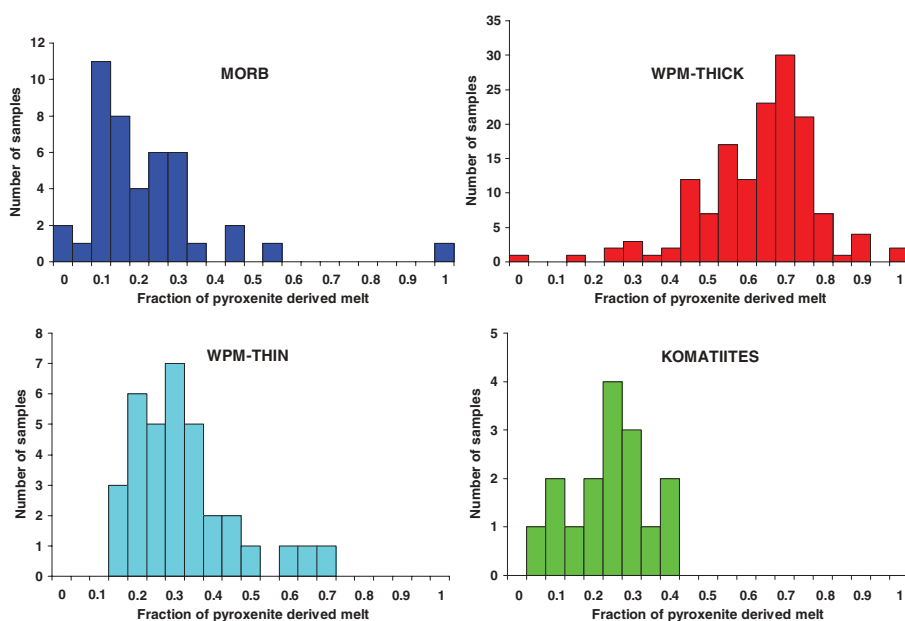


**Fig. 4.** Estimated amounts of pyroxenite-derived component in the parental melt for 229 samples of four different groups.

A high  $T_p$  is an important condition to maintain sufficient buoyancy of mantle plumes or any other upstream mantle flow, and this buoyancy limits the amount of dense eclogite that they can carry (35). Also, a high  $T_p$  affects mostly the proportion of peridotite-derived melt because fractional melting imposes a rather stringent upper limit to further melting at high melt fractions (36). High melt fractions are restricted to the eclogite and hybrid pyroxenite assemblages (26) (fig. S5). The peridotite assemblage produces lower melt fractions than pyroxenite (fig. S5) or eclogite (19, 25) at any given temperature and pressure, and its actual extent of melting therefore depends strongly on the specific  $T_p$ .

Lastly, why are the proportions of recycled component lower beneath mid-ocean ridges than in thick-lithosphere settings? We suggest several explanations: (i) Relatively low amount of dense recycled component in MORBs is limited by their  $T_p$ , which is too low to carry more. (ii) For statistical reasons, plumes are more likely to encounter more-common thick lithosphere than less-common thin lithosphere and few plumes impinge directly on ridges, so we are forced to deal with very-small-number statistics. (iii) Detroit seamount represents one case where a (Hawaiian) plume has encountered thin lithosphere and where our results do indicate a high fraction of recycled crust, similar to those found on the island of Hawaii on the thick lithosphere.

This amount is significantly higher than for Iceland, probably reflecting the effect of a higher  $T_p$  of the Hawaiian plume (4). (iv) The surface expression of a plume emplaced under thick lithosphere requires high  $T_p$ , which is necessary for carrying a significant amount of recycled crust (35), allowing melts to form at higher pressures than for ordinary peridotite (5, 25, 26), and melting a peridotite at higher pressures [e.g., komatiites (37)].

#### Heterogeneous versus homogeneous mantle.

The model presented here assumes that the recycled crustal component was not fully mixed with peridotite during subduction and mantle convection and thus that the formation of the olivine-free hybrid lithology may take place. On the other hand, homogenization of crustal material within the peridotite mantle should create a range of ultramafic lithologies with variable amounts of olivine, similar to a model by Kelemen *et al.* (20). Under these circumstances, the major-element contents of partial melts will correspond to the eutectic-like composition, buffered by the peridotite assemblage, whereas the compatible trace elements (Ni and Mn) will be controlled by the bulk partition coefficients of this assemblage and thus by the amount of olivine and pyroxene present in the system. Therefore, the amount of recycled crust can still be estimated on the basis of these trace elements, but their abundances will no longer correlate with the

buffered major elements (Si, Ca, and Al). For Hawaiian basalts, such correlations with Ni are present (5), which requires a strongly heterogeneous source.

**Input from Earth's core?** The Ni excess in mantle olivines from Siberian LIP (38) and the elevated Fe/Mn ratios in Hawaiian lavas (7) have been explained by input from Earth's core to the sources of mantle plumes. This suggestion is consistent with  $^{186}\text{Os}/^{188}\text{Os}$  ratios for some Hawaiian and Gorgona lavas (39) but is contradicted by the fact that concentrations of highly siderophile (Pt) and chalcophile (Cu) elements reported for Hawaiian basalts are not affected by this process (5). Our olivine data provide strong arguments against any notable core contribution to Ni or Fe excess in the sources of mantle-derived magmas. Cobalt does not show significant excess in olivines (Fig. 2 and fig. S3) and is effectively decoupled from Ni. As a result, the Ni/Co ratio in most Ni-rich mantle plume olivines exceeds 30 at the typical mantle Fo range of 89 to 91 (Fig. 2). This is not expected from a core contribution, because Ni/Co ratios for both mantle and core are almost equal and close to the chondritic value of about 20 (40). In addition, Ca is significantly depleted in many high-Ni and low-Mn olivines from the WPM-THICK group, which cannot be explained by core contribution. Lastly, the olivines from Gorgona komatiites, which do show significant excess in  $^{186}\text{Os}$  (39), do not indicate large anomalies in Ni and Mn/Fe, whereas Koolau lavas with the highest Ni excess and lowest Mn/Fe ratio in olivines do not show significant elevations in  $^{186}\text{Os}/^{188}\text{Os}$  ratios (39). This suggests complete decoupling of these potentially strong indicators of core-mantle exchange.

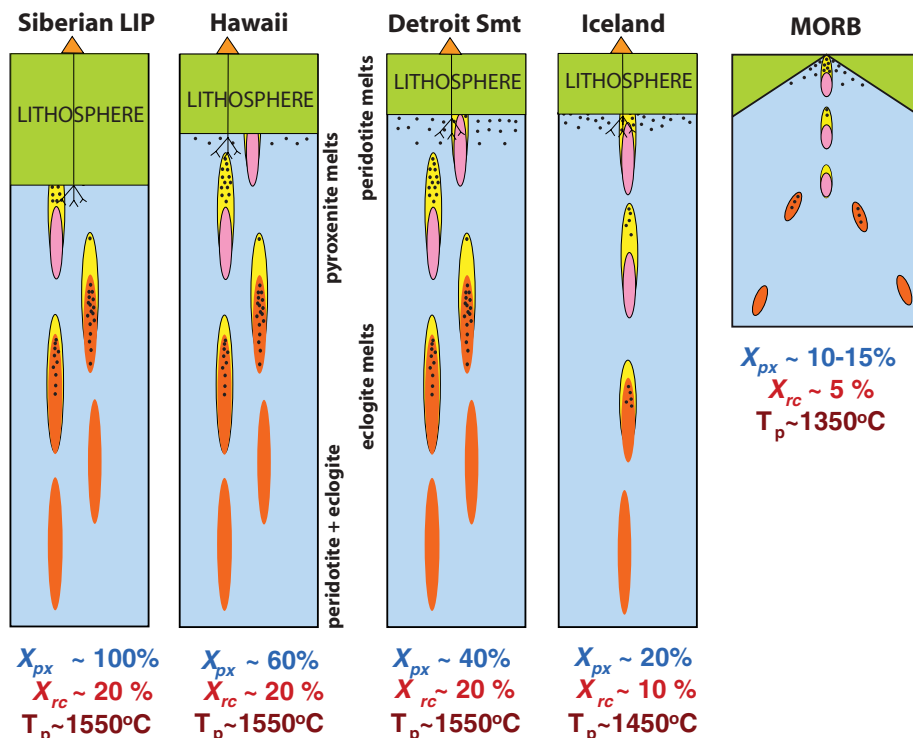


**Fig. 5.** Schematic model illustrating interplay between amount of recycled crust, thickness of lithosphere, and  $T_p$ . Blue, upwelling peridotitic mantle; red, recycled oceanic crust (eclogite with free  $\text{SiO}_2$  phase); black dots, melting; yellow, reaction zones forming hybrid pyroxenite; pink, refractory restite after eclogite melting; and green, lithosphere.  $X_{px}$ , amount of pyroxenite derived melt in the mixture with peridotite-derived melt, and  $X_{rc}$ , amount of recycled oceanic crust in the peridotitic mantle (42).

#### References and Notes

1. A. W. Hofmann, W. M. White, *Earth Planet. Sci. Lett.* **57**, 421 (1982).
2. A. W. Hofmann, in *The Mantle and Core*, vol. 2 of *Treatise on Geochemistry*, H. D. Holland, K. K. Turekian, Eds. (Elsevier, Amsterdam, 2003), p. 61.
3. E. H. Hauri, *Nature* **382**, 415 (1996).
4. C. Herzberg, M. J. O'Hara, *J. Petrol.* **43**, 1857 (2002).
5. A. V. Sobolev, A. W. Hofmann, S. V. Sobolev, I. K. Nikogosian, *Nature* **434**, 590 (2005).
6. Ni was first proposed as a monitor for replacement of olivine by pyroxene in (20).
7. M. Humayun, L. P. Qin, M. D. Norman, *Science* **306**, 91 (2004).
8. C. Herzberg, *Nature* **444**, 605 (2006).
9. S. M. Eggins, *Contrib. Mineral. Petrol.* **110**, 387 (1992).
10. Materials and methods are available on Science Online.
11. E. J. Jarosevich, J. A. Nelen, J. A. Norberg, *Geostand Newslett.* **4**, 43 (1980).
12. M. J. Walter, *J. Petrol.* **39**, 29 (1998).
13. V. S. Sobolev, A. V. Sobolev, *Dokl. Akad. Nauk SSSR* **237**, 437 (1977).
14. T. Kogiso, M. M. Hirschmann, D. J. Frost, *Earth Planet. Sci. Lett.* **216**, 603 (2003).
15. T. Kogiso, M. M. Hirschmann, M. Pertermann, *J. Petrol.* **45**, 2407 (2004).
16. T. Kogiso, M. Hirschmann, *Earth Planet. Sci. Lett.* **249**, 188 (2006).
17. A. Yasuda, T. Fujii, K. Kurita, *J. Geophys. Res.* **99**, 9401 (1994).
18. A. E. Ringwood, D. H. Green, *Tectonophysics* **3**, 383 (1966).

19. G. M. Yaxley, D. H. Green, *Schweiz. Mineral. Petrogr. Mitt.* **78**, 243 (1998).
20. P. B. Kelemen, S. R. Hart, S. Bernstein, *Earth Planet. Sci. Lett.* **164**, 387 (1998).
21. E. H. Hauri, M. D. Kurz, *Earth Planet. Sci. Lett.* **153**, 21 (1997).
22. J. C. Lassiter, E. H. Hauri, *Earth Planet. Sci. Lett.* **164**, 483 (1998).
23. R. P. Rapp, N. Shimizu, M. D. Norman, G. S. Applegate, *Chem. Geol.* **160**, 335 (1999).
24. D. S. Korzhinskii, *Theory of Metasomatic Zoning* (Clarendon, Oxford, 1970).
25. M. M. Hirschmann, E. M. Stolper, *Contrib. Mineral. Petrol.* **124**, 185 (1996).
26. G. M. Yaxley, *Contrib. Mineral. Petrol.* **139**, 326 (2000).
27. P. Beattie, *Contrib. Mineral. Petrol.* **115**, 103 (1993).
28. R. J. Kinzler, T. L. Grove, S. I. Recca, *Geochim. Cosmochim. Acta* **54**, 1255 (1990).
29. V. S. Kamenetsky *et al.*, *Geology* **29**, 243 (2001).
30. N. H. Sleep, *Annu. Rev. Earth Planet. Sci.* **20**, 19 (1992).
31. G. H. Gudfinnsson, D. C. Presnall, *J. Petrol.* **46**, 1645 (2005).
32. D. McKenzie, M. J. Bickle, *J. Phys. Earth* **38**, 511 (1990).
33. J. P. Morgan, *Geochem. Geophys. Geosystems* **2**, 2000GC000049 (2001).
34. G. Ito, J. J. Mahoney, *Earth Planet. Sci. Lett.* **230**, 29 (2005).
35. M. Pertermann, M. M. Hirschmann, *J. Petrol.* **44**, 2173 (2003).
36. I. Kushiro, *Annu. Rev. Earth Planet. Sci.* **29**, 71 (2001).
37. N. Arndt, *J. Geophys. Res.* **108**, XX (2003).
38. I. D. Ryabchikov, *Dokl. Earth Sci.* **389**, 437 (2003).
39. A. D. Brandon, R. J. Walker, *Earth Planet. Sci. Lett.* **232**, 211 (2005).
40. W. F. McDonough, S. S. Sun, *Chem. Geol.* **120**, 223 (1995).
41. L. V. Danyushevsky, *J. Volcanol. Geotherm. Res.* **110**, 265 (2001).
42. D. McKenzie, M. J. Bickle, *J. Petrol.* **29**, 625 (1988).
43. We thank B. Schulz-Dobrick for supervising purchase and establishing electron microprobe facility in MPI; Hawaiian Scientific Drilling Project team, Koolau Scientific Drilling Project team, Ocean Drilling Program team, A. T. Anderson, E. A. Mathez, and N. Gitahi for providing samples; E. J. Jarosevich for supplying microprobe standards; A. Yasevich for sample preparations and N. Groschopf for maintaining the electron microprobe. The paper benefited from discussions with M. Hirschmann, P. Kelemen, C. Herzberg, B. McDonough, I. Ryabchikov, L. Kogarko, A. Kadik, E. Galimov, V. Batanova. Constructive reviews of C. Herzberg, and P. Kelemen improved the

clarity of the manuscript. The study was supported by Wolfgang Paul Award of the Alexander von Humboldt Foundation, Germany, to A.V.S. Partial support from the following sources is also acknowledged: Russian Foundation for Basic Research (RFBR) grants 06-05-65234 and HLW-4264.2006.5 and Russian Academy of Sciences and Deutsche Forschungsgemeinschaft grant HO 1026/16-1 to A.V.S., RFBR grant 06-05-64651 to N.M.S., NSF grants EAR03-36874 to M.O.G. and EAR-0105557 to F.A.F., and Netherlands Research Center for Integrated Solid Earth Science grant 6.2.12 to I.K.N. This is School of Ocean and Earth Science and Technology, University of Hawaii, contribution no. 7104.

#### Supporting Online Material

[www.sciencemag.org/cgi/content/full/1138113/DC1](http://www.sciencemag.org/cgi/content/full/1138113/DC1)

SOM Text

Figs. S1 to S5

Tables S1 to S4

Data set

29 November 2006; accepted 16 March 2007

Published online 29 March 2007;

10.1126/science.1138113

Include this information when citing this paper.

# Genes Required for Mitotic Spindle Assembly in *Drosophila* S2 Cells

Gohta Goshima,<sup>1,3\*</sup> Roy Wollman,<sup>2,3</sup> Sarah S. Goodwin,<sup>1</sup> Nan Zhang,<sup>1</sup> Jonathan M. Scholey,<sup>2</sup> Ronald D. Vale,<sup>1,3†</sup> Nico Stuurman<sup>1,3</sup>

The formation of a metaphase spindle, a bipolar microtubule array with centrally aligned chromosomes, is a prerequisite for the faithful segregation of a cell's genetic material. Using a full-genome RNA interference screen of *Drosophila* S2 cells, we identified about 200 genes that contribute to spindle assembly, more than half of which were unexpected. The screen, in combination with a variety of secondary assays, led to new insights into how spindle microtubules are generated; how centrosomes are positioned; and how centrioles, centrosomes, and kinetochores are assembled.

The diamond-shaped mitotic spindle has become one of the most widely recognized images in biology, emblematic of life's propagation through cell division. In higher eukaryotes, the process of spindle formation begins after nuclear envelope breakdown (NEB) when microtubules (MTs), generated both from centrosomes and from the vicinity of chromatin, are organized into a bipolar array (1–5). Sister chromatids bind to MTs emanating from opposite poles, are aligned in the middle of the bipolar MT network, and then ultimately separate and move apart during anaphase. Failures early in mitosis result in the formation of an abnormal metaphase

spindle, which can lead to mitotic delay and, potentially, chromosome missegregation during the ensuing anaphase.

To understand the mechanism of metaphase spindle assembly, it is critical to identify the proteins required for this process and then dissect how they function. Many mitotic proteins have been identified through genetic and RNAi screens (6–10), but the inventory is likely incomplete. Here, we present a genome-wide screen for mitotic spindle morphology in *Drosophila* S2 cells and the functional analysis of unexpected genes discovered through the screen.

**Identification of genes involved in metaphase spindle formation by high-throughput microscopy.** Because the percentage of S2 cells in mitosis is low (~1%), we conducted our RNAi screen in the presence of dsRNA (double-stranded RNA) to Cdc27 (a subunit of the anaphase-promoting complex) to delay anaphase and thereby increase the percentage of metaphase cells (~10% of the population). Thus, our screen was designed to investigate the assembly of the metaphase spindle, but not anaphase or cytokinesis. We also rescreened the

final hits without Cdc27 RNAi-induced mitotic arrest. The majority (88%) showed identical phenotypes, although a few genes only manifest clear phenotypes under conditions of mitotic arrest (table S1).

Using our custom, full-genome (14,425 genes) *Drosophila* RNAi library (11), we treated S2 cells with dsRNA for 4 days, conditions that generally reduce protein levels by >80% (12, 13). After dsRNA treatment, cells were fixed and stained for DNA,  $\gamma$ -tubulin, MT, and phosphohistone H3 (pH3) in 96 well plates, and about 40 sites per well were imaged by automated microscopy with a high numerical aperture air objective to obtain relatively high-resolution images of mitotic spindles (Fig. 1A). To reduce the complexity of this large amount of image data, a custom computer code was used to identify, crop, and arrange mitotic spindles into galleries, which were then blindly scored by an observer (Fig. 1B and fig. S1). In addition, computer algorithms measured eight parameters of spindle shape, as well as the intensity of  $\gamma$ -tubulin, cell number, and mitotic index (Fig. 1C) (11). More than 4,000,000 spindles were analyzed in this screen.

Before beginning this screen, we annotated 49 genes that produce mitotic defects in S2 cells (table S2). Of these 49 genes, 45 were identified as hits in the primary screen, indicating a high success rate of identifying mitotic phenotypes. However, our final list of genes should not be considered as a complete or universal inventory, because genes can be missed (particularly those with subtle phenotypes), and some phenotypes (or lack thereof) may be specific to S2 cells. False positives by off-target effects of dsRNA can occur in RNAi screens (14, 15), so precautions were taken to minimize gene overlap in the dsRNA design, and all unexpected hits were confirmed with another dsRNA that had no overlap with the first dsRNA (11). To learn more about the functions of interesting genes,

<sup>1</sup>Howard Hughes Medical Institute and the Department of Cellular and Molecular Pharmacology, University of California, San Francisco, 600 16th Street, San Francisco, CA 94158, USA. <sup>2</sup>Department of Molecular and Cellular Biology, University of California, Davis, One Shields Avenue, 3203 Life Sciences, Davis, CA 95616, USA. <sup>3</sup>Physiology Course, Marine Biological Laboratory, 7 MBL Street, Woods Hole, MA 02543, USA.

\*Present address: Institute for Advanced Research, Nagoya University, Furo-cho, Chikusa-ku, Nagoya, 464-8601, Japan.

†To whom correspondence should be addressed. E-mail: [vale@cmp.ucsf.edu](mailto:vale@cmp.ucsf.edu)